frontiers | Frontiers in Earth Science

TYPE Original Research
PUBLISHED 07 June 2024
DOI 10.3389/feart.2024.1372839

OPEN ACCESS

EDITED BY
Li Ren,
Sichuan University, China

REVIEWED BY
Jianfeng Liu,
Sichuan University, China
Haichun Ma,
Hefei University of Technology, China

*CORRESPONDENCE
Shisen Zhao,
zhaoshisen@cumt.edu.cn

RECEIVED 18 January 2024
ACCEPTED 07 May 2024
PUBLISHED 07 June 2024

CITATION
Liu Y, Li Z, Zhao S, Jiang J and Yuan C (2024), Effects of inclination angle and confining pressure on triaxial unloading-induced slip behaviors of shale fractures.
Front. Earth Sci. 12:1372839.
doi: 10.3389/feart.2024.1372839

Effects of inclination angle and confining pressure on triaxial unloading-induced slip behaviors of shale fractures

Yi Liu[1,2], Zihan Li[3], Shisen Zhao[1]*, Jian Jiang[1] and Chao Yuan[4]

[1]School of Mechanics and Civil Engineering, China University of Mining and Technology, Xuzhou, China, [2]Jinan Rail Transit Group Co. Ltd., Jinan, China, [3]Shandong Experimental High School, Jinan, China, [4]School of Civil Engineering, Shandong University, Jinan, China

To explore the effects of fracture inclination angle θ and confining pressure σ_{3t} on the slip behaviors and friction properties of fractures, the triaxial unloading-induced slip experiments were performed on the shale fractures. The results show that the σ_{3t} controls the slip modes of fractures, while the θ affects the occurrence of the stick-slip events during the quasi-static slip stage. With the increase in σ_{3t}, the main slip modes of fracture transform from the stable-slip to stick-slip, and eventually to the creep-slip. The increase in θ facilitated the occurrence of stick-slip events. As the θ increased from 30° to 50°, the number of stick-slip events increased from 0 to 3 and from 2 to 4 for σ_{3t} = 10 MPa and 20 MPa, respectively. For σ_{3t} = 40 MPa, no stick-slip event occurred in the slipping process. The θ and σ_{3t} have great effects on interaction modes between asperities, which directly affected the friction properties of fractures. With increasing σ_{3t}, the void spaces between the asperities were further compacted, resulting in the transition of asperity interaction from overriding mode to shear-off mode. The transition of asperity interaction model therefore brought about the weakening of friction coefficient at the activation point and the onset of dynamic slip stage. There is a competitive relationship between the θ and σ_{3t} for the evolution of the friction properties of fractures. As the θ increase from 30° to 50°, for σ_{3t} = 10 MPa, the mean sheared-off thickness decreased from 0.502 mm to 0.433 mm, while for σ_{3t} = 40 MPa, the mean sheared-off thickness decreased from 0.505 mm to 0.319 mm. With the increment of θ, the anisotropy of joint roughness coefficient was weakened. We suggested that by adjusting the fracturing angle of hydro-fracturing, the earthquakes with large seismic moments may be effectively mitigated.

KEYWORDS

inclination angle, confining pressure, triaxial unloading-induced slip, slip behavior, shale fracture

1 Introduction

The shale gas has been a good alternative to traditional fossil energy due to its high thermal efficiency and low carbon emissions (Ma et al., 2017; Zhang et al., 2022; Sun et al., 2023). The large-scale exploitation of shale gas is expected to play a key role in alleviating energy crisis and environment pollution (Yuan et al., 2015; Gao et al., 2021; Jia et al., 2022; Liu et al., 2023). However, the natural shale

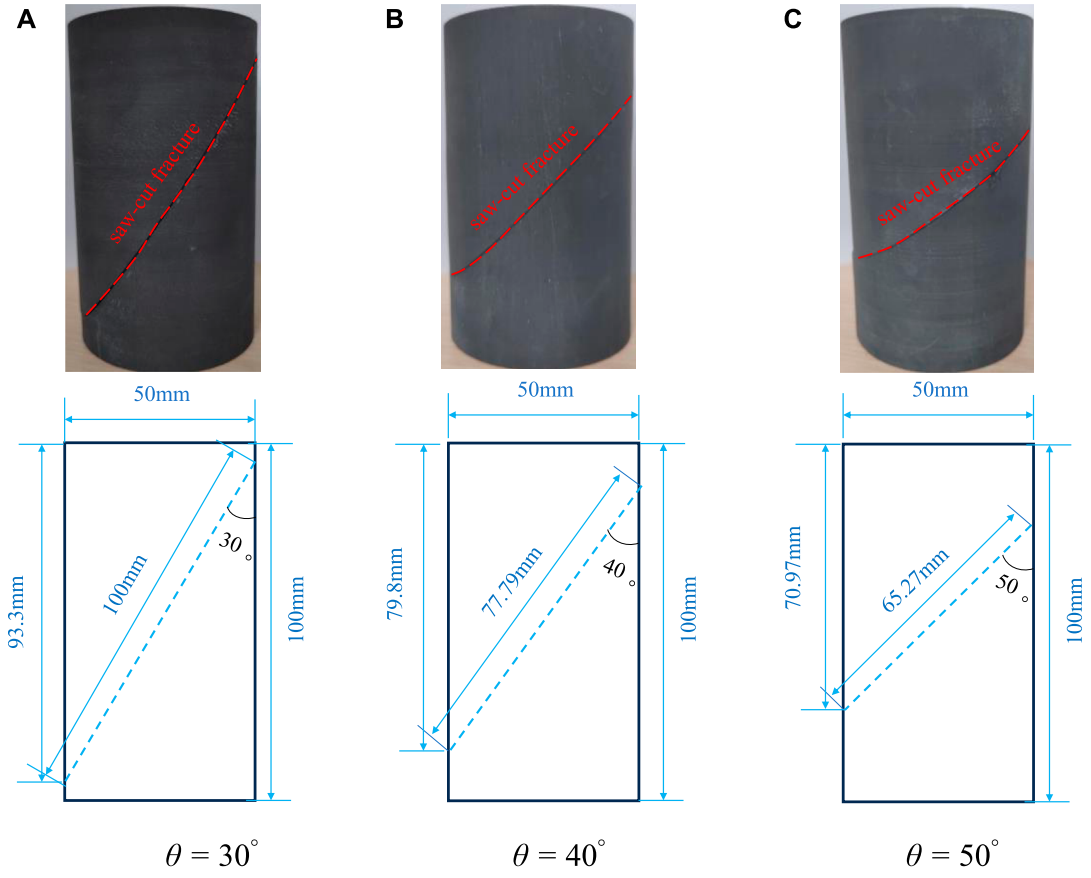

FIGURE 1
The geometrical size of the saw-cut shale fractures with different inclination angles θ: **(A)** θ = 30°, **(B)** θ = 40°, and **(C)** θ = 50°.

gas reservoirs are typically tight with a low porosity, and the hydro-fracturing technology is often employed to improve the permeability of reservoirs for efficient exploitation (Yasuhara et al., 2005; Zhang et al., 2016; Chen et al., 2021a; Yu et al., 2023). During the process of hydro-fracturing, massive fluid is injected into the reservoirs at high pressure to manufacture the tensile fractures (Zhang et al., 2016; Proctor et al., 2020). The increasing pore pressure due to fluid injection may perturb the *in situ* stress state of natural fractures and decrease the effective normal stress. The fault may be activated, and thereby leading to the occurrence of seismic activities (Guglielmi et al., 2015; Bao and Eaton, 2016; Elsworth et al., 2016; Ye and Ghassemi, 2020; Shi et al., 2022). Many countries have banned the hydro-fracturing related projects due to the dramatically increased frequency of earthquakes, for instance, the Germany, UK, and the France (Lee et al., 2016; Li et al., 2019; Evensen et al., 2022; Zhu et al., 2024). Despite of this, hydro-fracturing is still one of the most efficient and cleanest way to extract shale gas (Ferguson et al., 2021; Wu et al., 2021; Wang et al., 2022). The generated fracture networks due to hydro-fracturing leads to the dramatical increase in the permeability of shale formation by serval orders of magnitudes, which has significantly improved the efficiency of shale gas recovery (Liu et al., 2021; Zhang et al., 2021). Thus, there is a great need to unravel the mechanism of fracture activation related to the hydro-fracturing, so as to identify and mitigate the induced seismicity.

FIGURE 2
The MTS 815.02 rock mechanics testing system.

Many studies have been conducted to investigate the activation and frictional behaviors of fractures (Guglielmi et al., 2015; Scuderi

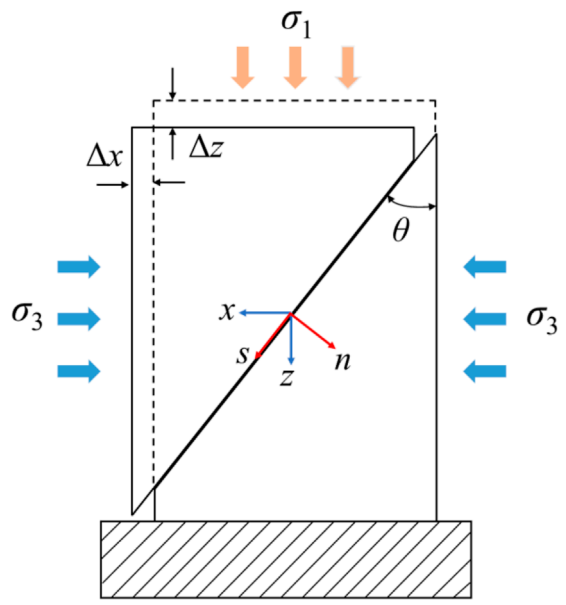

FIGURE 3
The schematic view of sample deformation during the slip process (after Ye and Ghassemi, 2018).

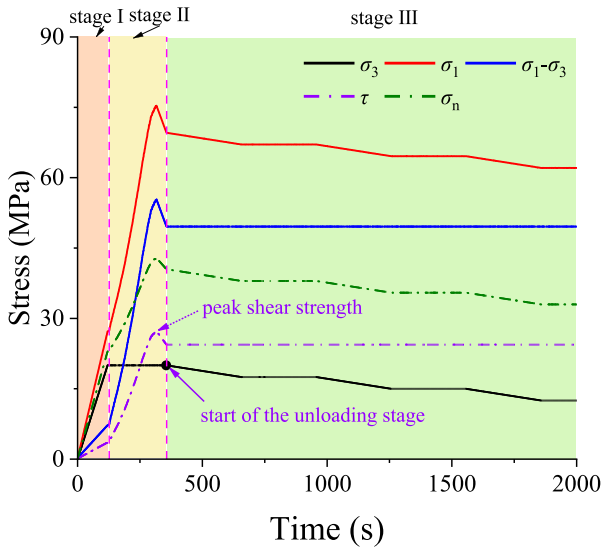

FIGURE 4
Evolutions of the confining pressure σ_3, axial stress σ_1, deviator stress σ_1 - σ_3, shear stress τ and normal stress σ_n in the unloading-induced slip experiments.

and Colletttini, 2018; An et al., 2020a; An et al., 2020b; Zhang et al., 2022). An et al. (2020a), An et al. (2020b) performed the frictional experiments on the shale fractures using the triaxial shearing apparatus, and the effects of temperature, pore pressure as well as the mineral composition were considered. They found that increasing the pore pressure may favor the fractures slipping in a stable state, and the slip modes of fractures were mainly controlled by proportion of the phyllosilicate and total organic carbon. Ji et al. (2019) carried out the triaxial unloading-induced shear tests on the

TABLE 1 The experimental conditions for nine saw-cut shale samples.

Num	Inclination angle (°)	Confining pressure (MPa)
#1	30	10
#2	30	20
#3	30	40
#4	40	10
#5	40	20
#6	40	40
#7	50	10
#8	50	20
#9	50	40

smooth and rough granite fractures, and their results showed that the stability of fracture was dominated by the ratio of system stiffness to fracture weakening rate. Mei and Wu (2021) conducted the direct-shear experiments on the fractures with simulated polycarbonate layer, and the influence of normal stress on the slip behaviors and asperity evolution was investigated. They found that with the decrease in normal stress, there was a transition of slip behavior from stick-slip to stable sliding. Liu et al. (2023) explored the effect of simultaneous unloading of normal stress and shear stress on the activation of sandstone fractures with using direct shear apparatus. They proposed that the slip modes of fractures were controlled by the ratio of the unloading rate of shear stress to that of normal stress, and decrease in the ratio may weaken the stability of fracture. However, most of these studies focus on the fractures at shallow depth. With increasing the depth, the confining pressure that the fracture suffers increases nearly linearly. The buried depth of shale gas reservoir detected in Sichuan, China, reaches up to 4 km, where the confining pressure is as high as 40 MPa (Sun et al., 2021; Zeng et al., 2022). Previous studies showed that the increment of confining pressure may strengthen the compaction effect between mineral particles and prolong the damage phase, thus leading to the variation in shear properties of fracture (Liu et al., 2023; Huang et al., 2023). Zhang et al. (2023) found that with increasing confining pressure, the process of strain softening was facilitated while the failure strain was strongly restricted. Therefore, it is necessary to study the effect of confining pressure on activation and subsequent slip behaviors of fractures.

The natural fractures or faults show anisotropic properties, which can be determined by two parameters, i.e., the strike and dip angle (Huang et al., 2021). In different shale gas reservoirs, the dip angles of natural fractures are variable due to tectonic movements (Chattopadhyay et al., 2020). The *in situ* stress state of these fractures and the disturbance stress acting on the fracture surfaces during hydro-fracturing are different. The dip angle of natural fracture can be directly reflected as the inclination angle in the laboratory test (see Figure 1). Most of the inclination angles used in the experiments are between 20 and 55°, so as to prevent the generation of new cracks

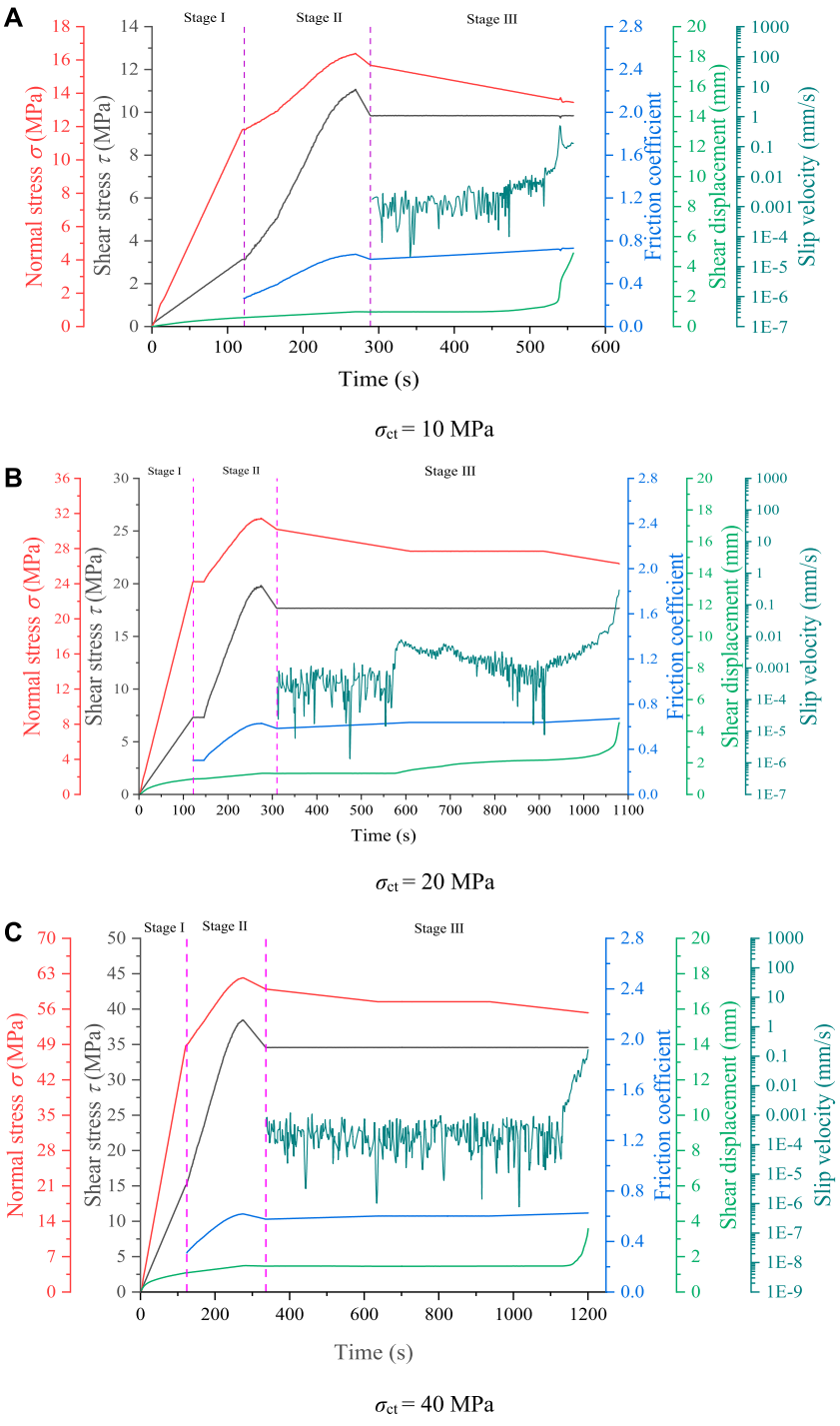

FIGURE 5
Evolutions of mechanical and kinematic parameters during the slip process under different confining pressures σ_{ct} for the fractures with θ = 30°: **(A)** σ_{ct} = 10 MPa; **(B)** σ_{ct} = 20 MPa; **(C)** σ_{ct} = 40 MPa.

in rock matrix (Brady and Brown, 2006; Zhang et al., 2022; Ji et al., 2022b). Some scholars have investigated the effect of inclination angle on the shear properties of fractures (Giorgetti et al., 2019; Chen et al., 2021b; Yue et al., 2022). Yue et al. (2022) explored the effect of inclination angle on the shear behavior and damage mode of fractures, and found that the damage degree and shear strength were strongly correlated with the relative position between the inclination angle and the shear direction. Chen et al. (2021)conducted shear tests on sandstone specimens with variable joint inclination angles. Their results demonstrated that with the increase in inclination angle, the number of shearing cracks gradually decreased, while some tensile cracks were formed due to the local stress rotation (Giorgetti et al., 2019). However, there are rare studies to explore the influence of fracture inclination angle on slip characteristics of

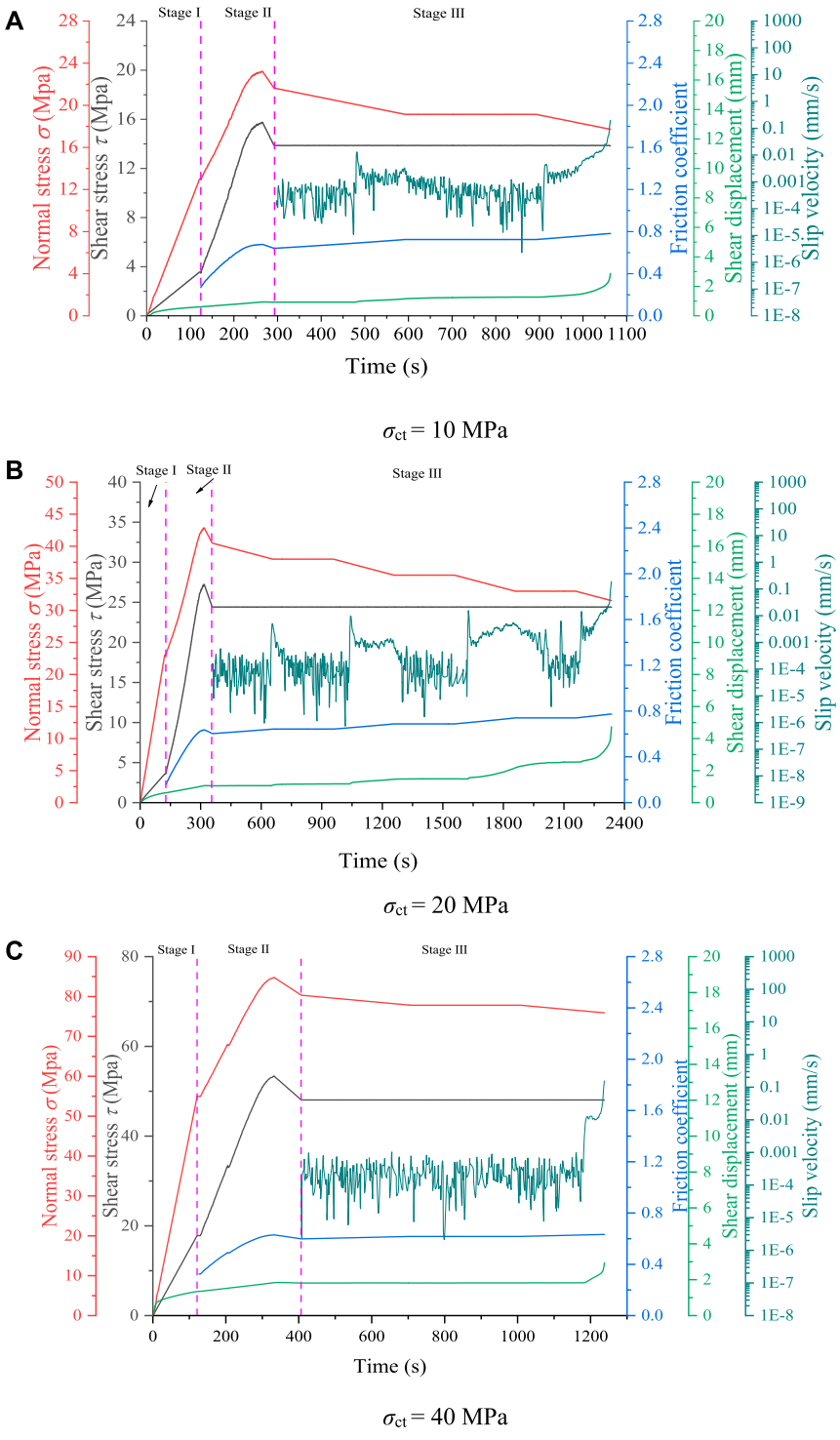

FIGURE 6
Evolutions of mechanical and kinematic parameters during the slip process under different σ_{ct} for the fractures with θ = 40°: **(A)** σ_{ct} = 10 MPa; **(B)** σ_{ct} = 20 MPa; **(C)** σ_{ct} = 40 MPa.

fractures. Previous studies have shown that there were competing effects between these factors on fracture activation as well as slip behavior (An et al., 2020b; Ji et al., 2022; Zhang et al., 2022). It is imperative to conduct thorough investigation on the combined effects of inclination angle and confining pressure on the slip behaviors of fractures.

In this study, shale fractures with different inclination angles were employed to perform the triaxial unloading-induced slip experiments under different confining pressures. The normal stress applied on the fracture surfaces was stepwise unloaded as perturbed stress to activate the fractures. The effects of confining pressure and inclination angles on the fracture activation, slip modes, and friction

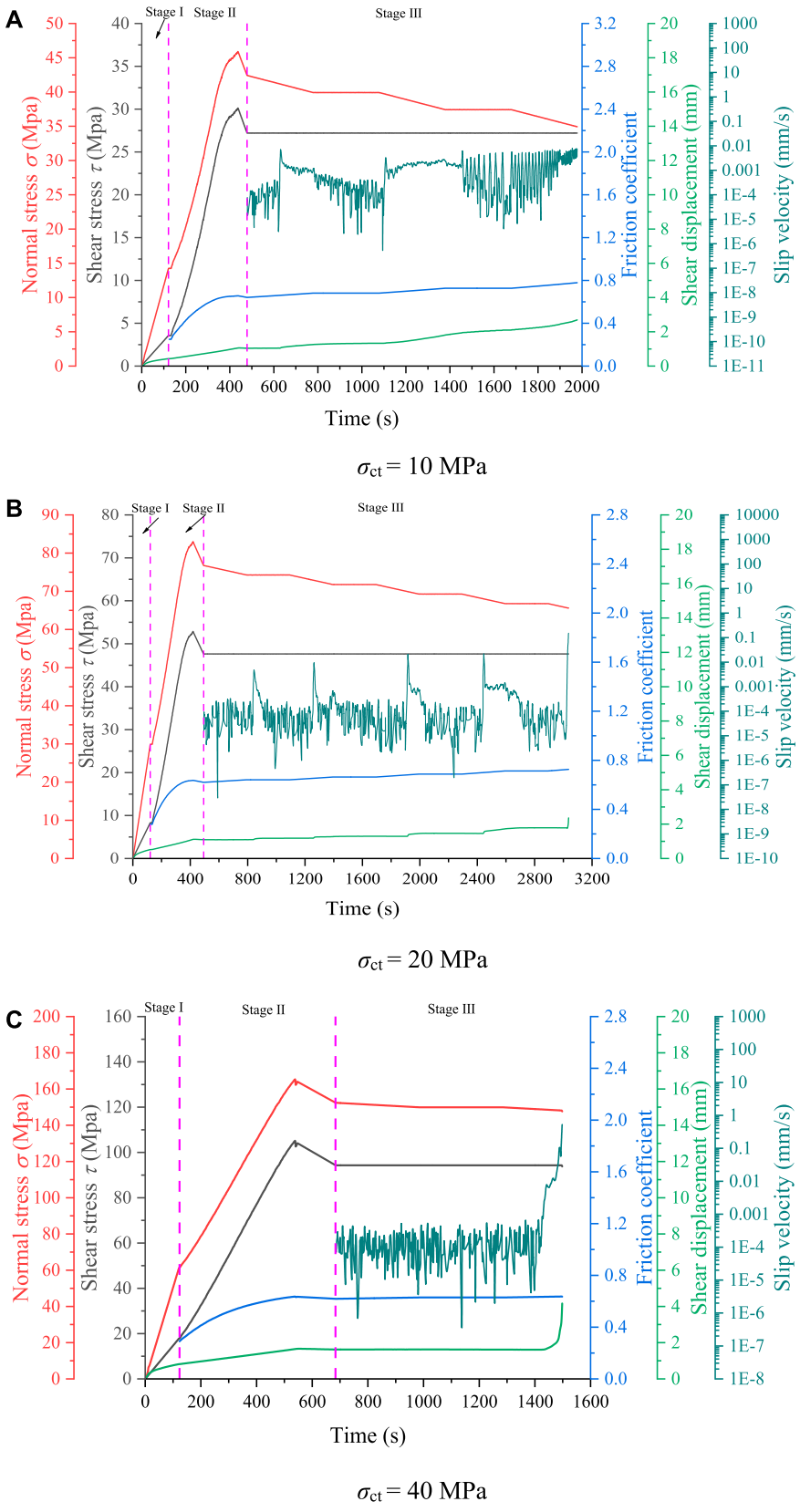

FIGURE 7
Evolutions of mechanical and kinematic parameters during the slip process under different σ_{ct} for the fractures with θ = 50°: **(A)** σ_{ct} = 10 MPa; **(B)** σ_{ct} = 20 MPa; **(C)** σ_{ct} = 40 MPa.

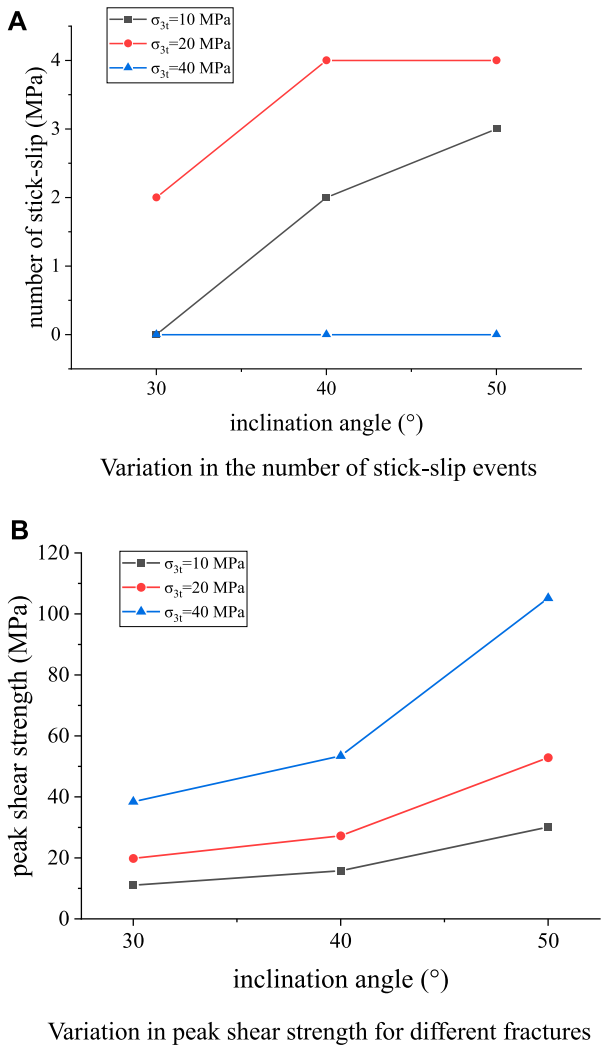

FIGURE 8
Number of stick-slip events in the quasi-static slip stage and the peak shear strength of fractures with different θ: **(A)** Variation in the number of stick-slip events; **(B)** Variation in peak shear strength for different fractures.

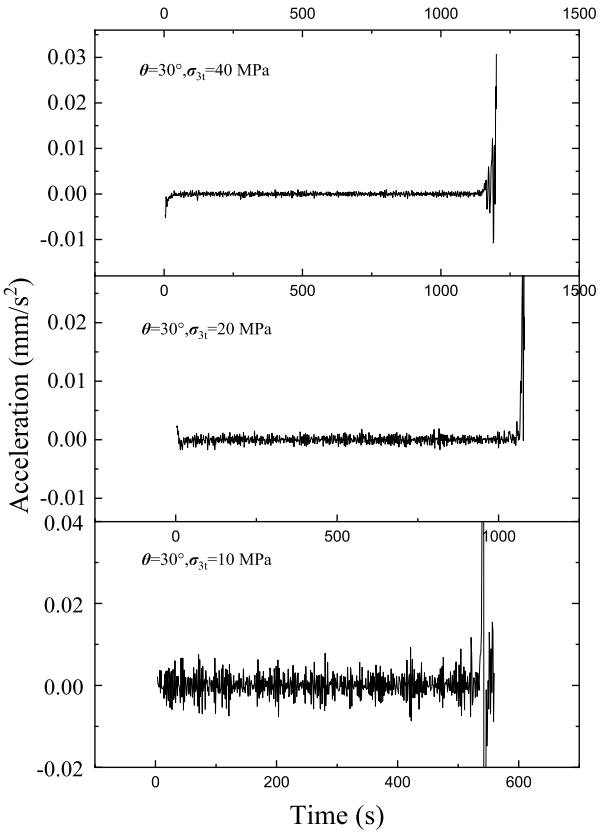

FIGURE 9
Variation in acceleration during the slip process for the fractures with $\theta = 30^{\circ}$.

characteristics were investigated in detail. The damage modes of fractures and the evolution of joint roughness coefficient (JRC) tensors were explored. Finally, the mechanism of fracture activation and implication for shale gas exploitation were discussed.

2 Materials and methods

2.1 Sample preparation and experimental setup

The shale was cored from Longmaxi shale formation in Sichuan, China, and consists of 43% quartz, 18.3% calcite, 14.8% illite, 13.4% chlorite, and 10.5% albite according to the X-ray diffraction (XRD). Nine cylindrical shale specimens with a height of 100 mm and a diameter of 50 mm were made to manufacture the saw-cut fracture samples with different inclination angles θ (see Figure 1). The samples were then divided into three groups according to the θ, and each group contains three saw-cut fracture samples with the same θ. The θ was set to be 30°, 40°, and 50° for three groups, respectively. To minimize the influence of roughness on the activation and slip process of fractures, all the fracture surfaces were polished with fine-grained sandpaper (Ji et al., 2022).

As shown in Figure 2, the triaxial unloading-induced fracture slip experiments were performing on the MTS 815.02 rock mechanics testing system, which has been widely adopted to investigate the fracture activation due to its high performance in servo controlling (Ishibashi et al., 2018; Wang et al., 2020; Bijay and Ghazanfari, 2021; Ji et al., 2023; Zhu et al., 2023). The servo controlling system enables the real-time adjustment of shear stress τ and normal stress σ_n applied on the fracture surface. Figure 3 depicts the stress state of the sample in the triaxial pressure chamber, and the τ and σ_n can be calculated as:

$$\tau = (\sigma_1 - \sigma_3)\sin\theta\cos\theta \quad (1)$$

$$\sigma_n = \sigma_3 + (\sigma_1 - \sigma_3)\sin^2\theta \quad (2)$$

where σ_1 is the axial stress, σ_3 is the confining pressure. According to Coulomb failure criterion and Terzaghi effective stress principle (Nur and Byerlee, 1971; Lade and De Boer, 1997; Wang et al., 2020), with the increase in pore pressure P_p or decrease in σ_n, the fracture

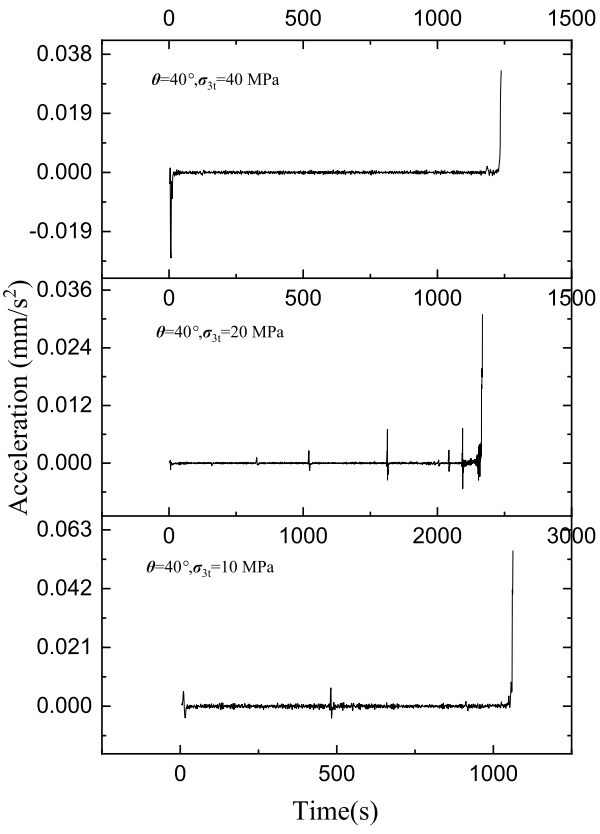

FIGURE 10
Variation in acceleration during the slip process for the fractures with θ = 40°.

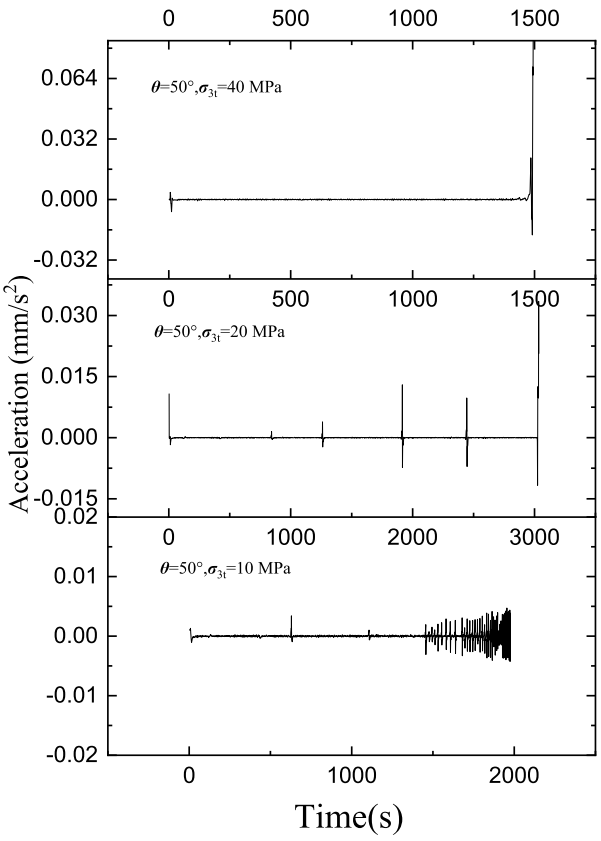

FIGURE 11
Variation in acceleration during the slip process for the fractures with θ = 50°.

may be activated to slip once the τ resolved along the fracture plane exceeds the shear strength τ_s. This can be described as (Passelègue et al., 2018):

$$\tau > \tau_s = \mu\left(\sigma_n - P_p\right) \tag{3}$$

where μ is the friction coefficient. In our study, the scheme of fluid injection was not employed (i.e., P_p = 0). Thus, Eq. 3 can be demonstrated as (Ji et al., 2019):

$$\tau > \tau_s = \mu\sigma_n \tag{4}$$

Thus, when the deviator stress σ_1 - σ_3 is held constant, the decrease in σ_3 can lead to the decrease in σ_n. In our study, the driving mode of unloading σ_3 was chosen as an alternative to increasing P_p to induce the slip of fracture.

The displacements of fracture in both parallel d_s and normal d_n to the shear direction can be calculated based on the axial deformation Δz and radial deformation Δx of the sawcut sample (Ye and Ghassemi, 2018):

$$d_n = \Delta z \sin\theta - \Delta x \cos\theta \tag{5}$$

$$d_s = \Delta z \cos\theta + \Delta x \sin\theta \tag{6}$$

The Δz and Δx can be monitored by the sensors embedded in the piston and the circumferential extensometer, respectively. Both Δz and Δx were recorded at a sampling interval Δt of 1 s. The increment of d_s within Δt was defined as Δd_s. The shear slip velocity v_s can be calculated as:

$$v_s = \Delta d_s / \Delta t \tag{7}$$

The acceleration a_s of fracture can be obtained as:

$$a_s = \Delta d_s / \Delta t^2 \tag{8}$$

In order to obtain the variation in the morphology of fracture surfaces after the fractures were activated and experienced shear slipping, the three-dimensional scanning system 3DSS was utilized. This scanning system has a resolution of ±1 μm in the z direction and ±20 μm in the x and y directions, respectively.

2.2 Experimental procedures

Figure 4 depicts the typical evolutions of the confining pressure σ_3, axial stress σ_1, deviator stress σ_1 - σ_3, shear stress τ and normal stress σ_n in the unloading-induced slip experiments. And the loading paths of stresses throughout the triaxial unloading-induced fracture slip experiment can be divided into three stages. The stages I and II constitute the displacement-driven process, and stage III is the unloading-driven slip process. In the stage I, the σ_3 was loaded to the target value σ_{3t} at a constant rate U_c for 2 min, while the

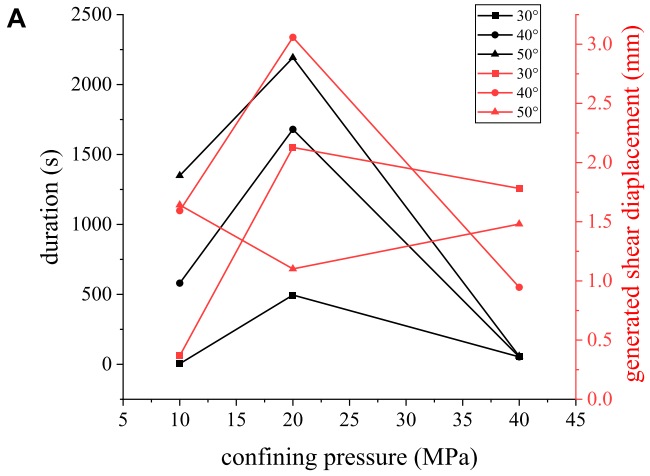

Duration of quasi-static slip stage and the generated shear displacement during the stage for fractures under different σ_{ct}

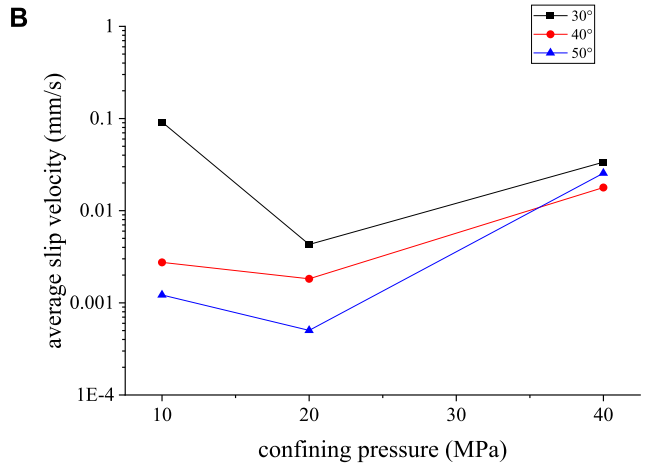

Average slip velocity during the quasi-static slip stage for fractures under different σ_{ct}

FIGURE 12
Duration, generated shear displacement and average slip velocity during the quasi-static slip stage for fractures under different σ_{ct}: **(A)** Duration of quasi-static slip stage and the generated shear displacement during the stage for fractures under different σ_{ct}; **(B)** Average slip velocity during the quasi-static slip stage for fractures under different σ_{ct}.

σ_1 - σ_3 was loaded at a smaller loading rate of U_{ca} than σ_1 to avoid the occurrence of fracture activation. Here, the maximum of σ_3 was set to 40 MPa to explore the slip characteristics of fracture under large buried depth. And σ_{3t} was set to be 10 MPa, 20 MPa, and 40 MPa to investigate the effect of confining pressure (or buried depth) on the fracture activation. In the stage II, the σ_3 was held constant at σ_{3t}, and the σ_1 - σ_3 was gradually loaded by moving the piston downward at a constant rate of 0.001 mm/s to make the τ applied on the fracture reach the peak shear strength τ_p. After that, the τ was reduced to $0.85\tau_p$ through moving the piston upward at a speed of 0.001 mm/s, where the fracture is viewed as being in a critical stress state. In the stage III, σ_1 - σ_3 was maintained constant, and the σ_3 was unloaded in steps at a fixed rate of 0.5 MPa/min for 5 min, followed by being held for another 5 min. This unloading-holding-unloading process was repeated until the fracture is destabilized. The experimental conditions for each sample can be found in detail in Table 1.

3 Results and analysis

3.1 Slip behaviors of fractures

The variations in the mechanical parameters and kinematic parameters during the slip process of the fractures were shown in Figures 5–7. In the displacement-driven processes, all the fractures were loaded to the τ_p in a stable state. The τ_p was significantly enhanced by the increasing σ_{3t} (see Figure 8). As σ_{3t} increases from 10 MPa to 40 MPa, the τ_p of fractures with θ = 30° and 40° increased from 11.06 MPa to 38.43 MPa, 15.77 MPa–53.42 MPa, with increments of 27.37 MPa and 37.65 MPa, respectively. For the fracture with θ = 50°, the strengthening effect on τ_p was further amplified, and the τ_p increased from 30.12 MPa to 105.19 MPa, with an increment of 75.07 MPa. Under the same σ_{3t}, the fracture with θ = 50° had the largest shear strength, followed by θ = 40° and 30°.

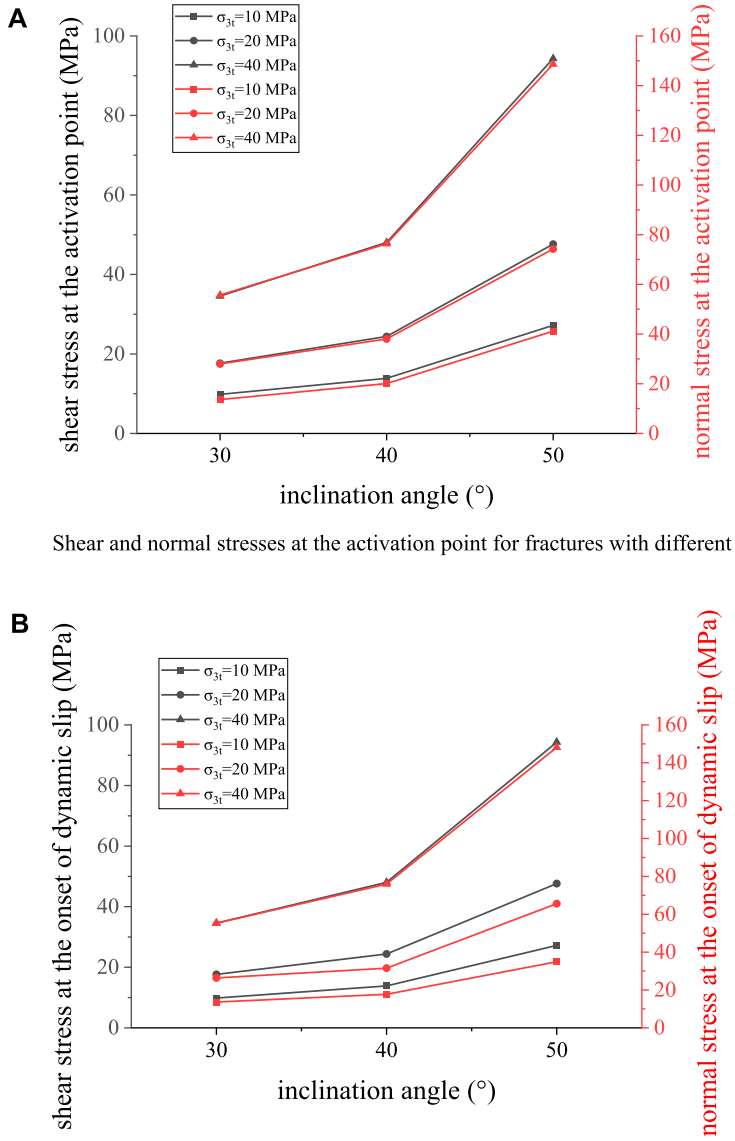

FIGURE 13
Shear and normal stresses at the activation point and the onset of dynamic slip stage for fractures with different θ: **(A)** Shear and normal stresses at the activation point for fractures with different θ; **(B)** Shear and normal stresses at the onset of dynamic slip stage for fractures with different θ.

After entering the unloading-driven process, the decrease of σ_3 perturbed the initially stable stress state of fractures and the fractures may be activated. Eventually, the imbalanced stress applied on the fractures forced the fractures to enter the dynamic slip stage. Taking the sample #5 as an example, in the stage III, the fracture was activated to slip at $t = 652.54$ s and subsequently entered the quasi-static slip stage. During the quasi-static slip stage, four stick-slip events occurred. Finally, the fracture slipped unstably and entered the dynamic slip stage at $t = 2331.66$ s. Here, the activation point was defined as the time point when the slip velocity of fracture is larger than 0.003 mm/s, while the start of dynamic slip stage is defined as the time point when the slip velocity of fracture is larger than 0.1 mm/s (Wang et al., 2019; Liu B. et al., 2023). The duration from the activation point to the start of dynamic slip stage was characterized as the quasi-static slip stage. During the quasi-static slip stage, the slip velocity of fracture may increase suddenly and then decrease slowly, accompanied by large acceleration (see Figures 9–11). This event is defined as a stick-slip event (Ji et al., 2023).

There were significant differences in the slip behaviors between fractures under the influence of σ_3 and θ. For the cases of $\theta = 30°$, when $\sigma_{3t} = 10$ MPa, the fracture steadily slipped and no stick-slip event occurred during the quasi-static slip stage. When $\sigma_{3t} = 20$ MPa, the fracture was activated at $t = 577.51$ s and then experienced the first stick-slip event subsequently. A total of two stick-slip events occurred during the quasi-static slip stage. The d_s showed a dramatical increase in each stick-slip event, and at the rest of the duration, the fractures remained almost

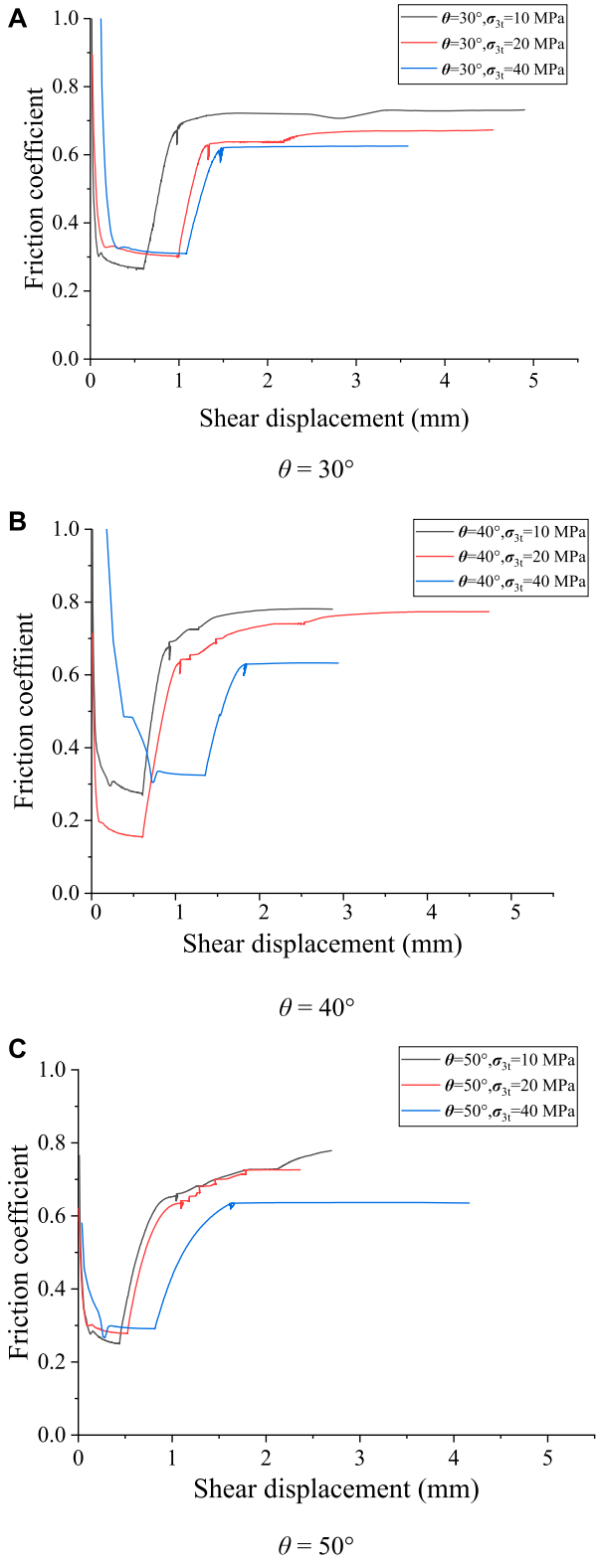

FIGURE 14
Friction coefficient versus shear displacement for the fractures with different θ: **(A)** θ = 30°; **(B)** θ = 40°; **(C)** θ = 50°.

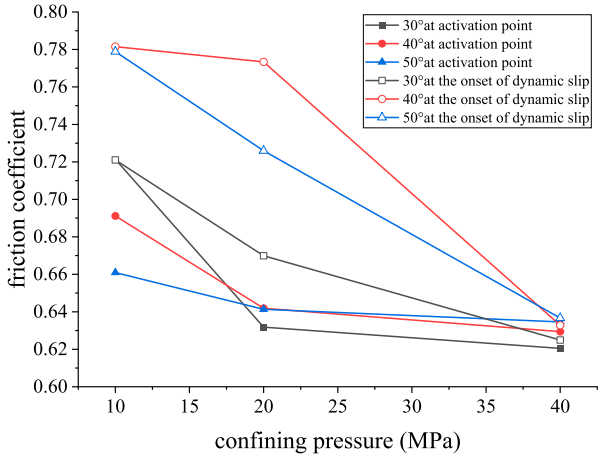

FIGURE 15
Variations in the friction coefficient at the activation point and the onset of dynamic slip stage *versus* σ_{ct} for fractures with different θ.

motionless (see Figure 6B). When σ_{3t} = 40 MPa, the fracture was activated at t = 1145.73 s and entered the dynamic slip stage at t = 1198.75 s. There was no stick-slip event during the quasi-static slip stage, and this stage only lasted for 53.02 s. The large σ_{3t} led to the tight engaging of the asperities between the upper and lower fracture surfaces. Therefore, the fracture was in a nearly static state before the activation point. Then, the slip velocity of the fracture increased rapidly to release the accumulated strain energy.

With the increase of θ, the slip modes of fractures did not change greatly, but the number of stick-slip events gradually increased for σ_{3t} = 10 MPa and 20 MPa (see Figure 8). For σ_{3t} = 10 MPa, the stick-slip events occurred 0, 2, and 3 times for the fractures with θ = 30°, 40°, and 50°, respectively. As shown in Figure 12, as the θ increased from 30° to 50°, the duration of quasi-static slip stage increased from 4.00 s to 1378.67 s, and the generated shear displacement d_s during this stage increased 0.37 mm–1.64 mm. While for σ_{3t} = 20 MPa, with increasing θ, the number of stick-slip events slightly increased. As the θ increased from 30° to 40°, the duration of quasi-static slip stage and the generated d_s increased from 495.30 s to 1679.12 s and from 2.13 mm to 3.06 mm, respectively. When the θ = 50°, 4 stick-slip events occurred during the quasi-static slip stage, and the stage reached the longest duration of 2192.13 s among the nine fractures. The duration of quasi-static slip stage for the fracture with θ = 30° was 4.4 times larger than that of θ = 50°. The reasons may be that the increase in θ results in the increase in σ_n applied on the fracture surface, so it is difficult for the asperities to override each other, and instead the asperities were sheared-off to release the strain energy. For σ_{3t} = 40 MPa, the stick-slip event was severely suppressed. With increasing the θ from 30° to 50°, the duration of quasi-static slip stage only slightly increased from 53.02 s to 58.03 s, and the generated d_s decreased from 1.78 mm to 1.48 mm. Figure 13 shows the τ and σ_n applied on the fracture at the activation point and the onset of dynamic slip stage, respectively. As the θ increases from

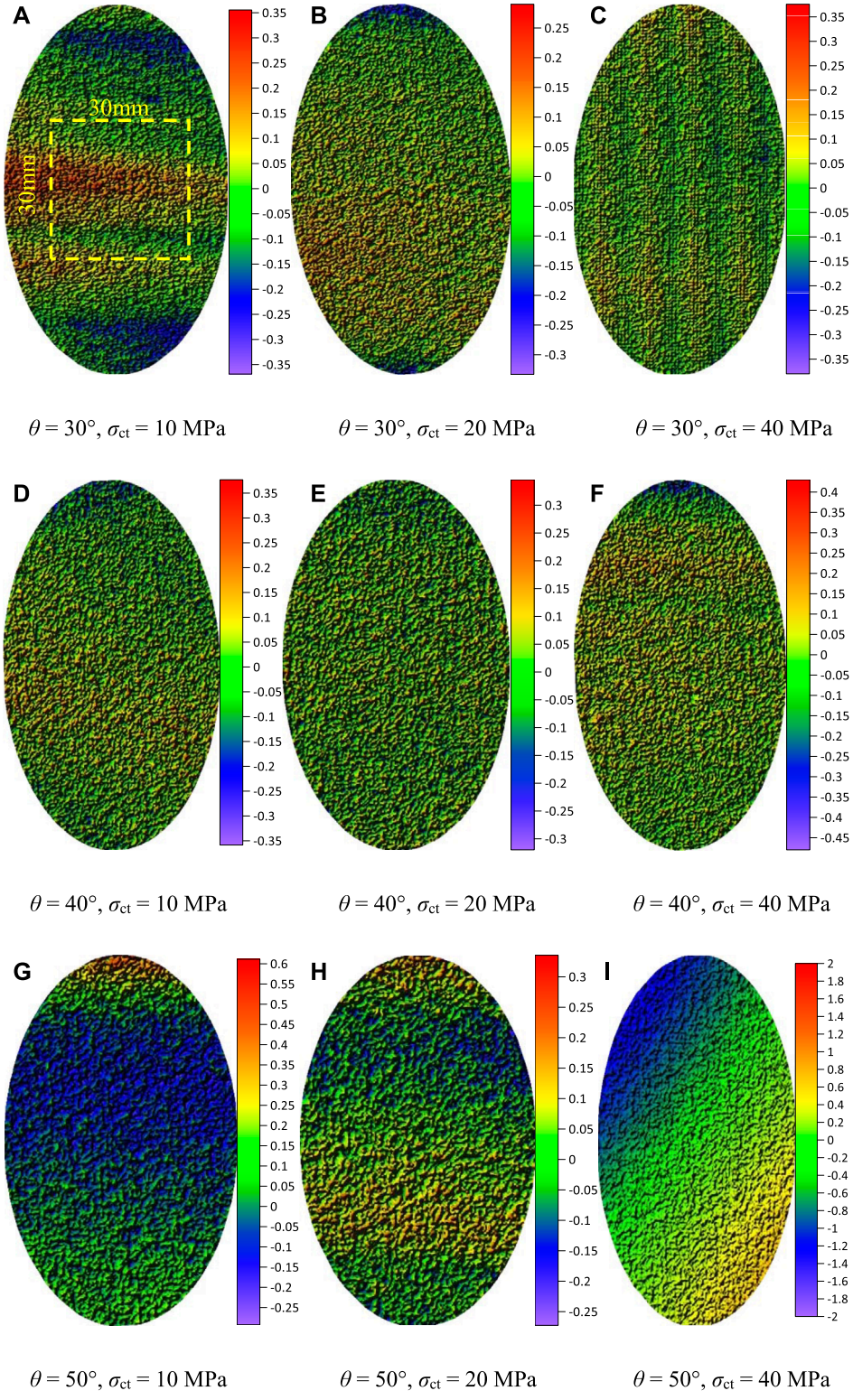

FIGURE 16
Morphology of fracture surfaces before experiments: **(A)** θ = 30°, σ_{ct} = 10 MPa; **(B)** θ = 30°, σ_{ct} = 20 MPa; **(C)** θ = 30°, σ_{ct} = 40 MPa; **(D)** θ = 40°, σ_{ct} = 10 MPa; **(E)** θ = 40°, σ_{ct} = 20 MPa; **(F)** θ = 40°, σ_{ct} = 40 MPa; **(G)** θ = 50°, σ_{ct} = 10 MPa; **(H)** θ = 50°, σ_{ct} = 20 MPa; **(I)** θ = 50°, σ_{ct} = 40 MPa.

30° to 50°, the τ increased 17.37 MPa and 59.77 MPa at the initiation point for σ_{3t} = 10 MPa and 40 MPa, respectively. At the onset of the dynamic slip stage, with increasing θ, both of τ and σ_n greatly increased.

3.2 Frictional characteristics of fractures

According to the Mohr-Coulomb failure principle, with the continuous unloading of σ_3, the Mohr circle representing the stress

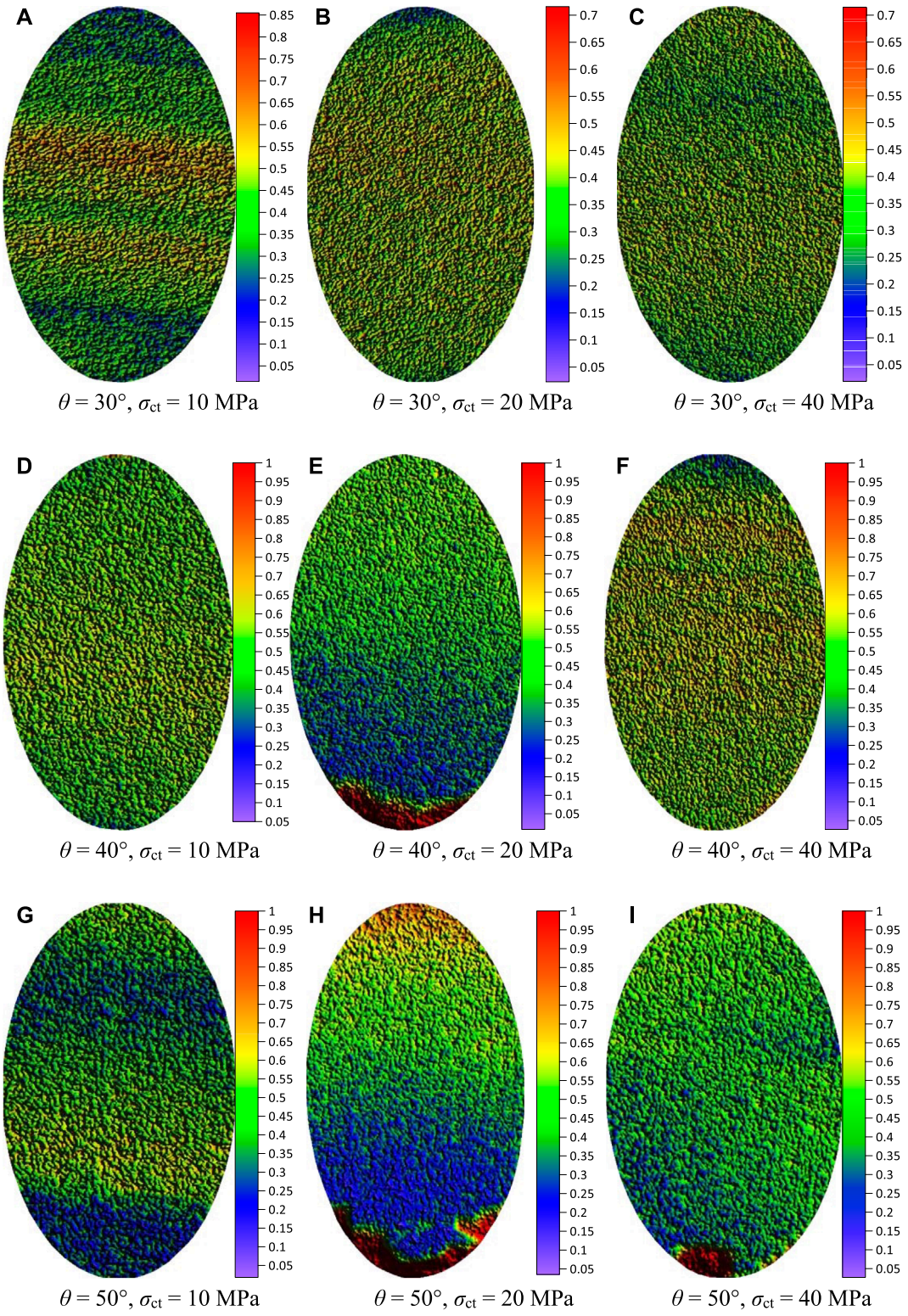

FIGURE 17
Morphology of fracture surfaces after experiments: **(A)** θ = 30°, σ_{ct} = 10 MPa; **(B)** θ = 30°, σ_{ct} = 20 MPa; **(C)** θ = 30°, σ_{ct} = 40 MPa; **(D)** θ = 40°, σ_{ct} = 10 MPa; **(E)** θ = 40°, σ_{ct} = 20 MPa; **(F)** θ = 40°, σ_{ct} = 40 MPa; **(G)** θ = 50°, σ_{ct} = 10 MPa; **(H)** θ = 50°, σ_{ct} = 20 MPa; **(I)** θ = 50°, σ_{ct} = 40 MPa.

state of fracture will move to the left. The fracture may be activated when the Mohr circle encounters the Coulomb failure envelope. Therefore, the μ is an important indicator of fracture instability.

Figure 14 shows the evolution of μ with d_s under different θ and σ_{3t}. In the displacement-driven process (stages I and II), the μ rapidly decreased due to the higher loading rate of σ_3 compared

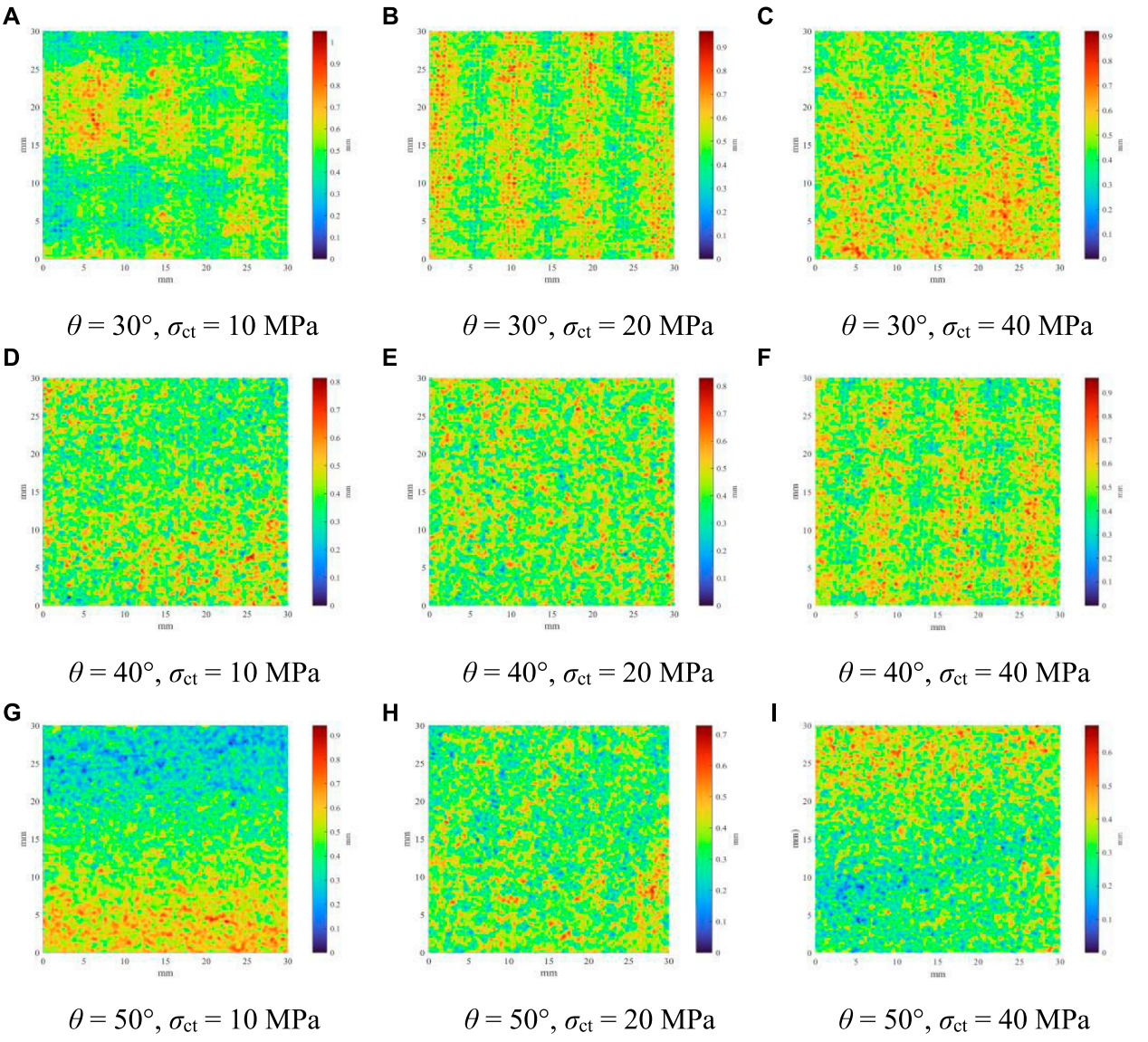

FIGURE 18
Thickness of sheared-off layer of fracture surfaces in the rectangular region (in Figure 16) after experiments: **(A)** θ = 30°, σ_{ct} = 10 MPa; **(B)** θ = 30°, σ_{ct} = 20 MPa; **(C)** θ = 30°, σ_{ct} = 40 MPa; **(D)** θ = 40°, σ_{ct} = 10 MPa; **(E)** θ = 40°, σ_{ct} = 20 MPa; **(F)** θ = 40°, σ_{ct} = 40 MPa; **(G)** θ = 50°, σ_{ct} = 10 MPa; **(H)** θ = 50°, σ_{ct} = 20 MPa; **(I)** θ = 50°, σ_{ct} = 40 MPa.

to σ_1. Then peak friction coefficient μ_p was reached simultaneously with τ_p under the sustained loading of σ_1. When the τ decreased from τ_p to $0.85\tau_p$, the μ experienced a slow decrease. As the shale samples were pressed continuously, it rebounded as the σ_1 decreased, resulting in the reduced d_s. Thus, many hysteresis loops can be found in Figure 14.

In the unloading-driven process (stage III), the stepwise unloading of σ_3 led to the increment of μ. Here, we defined the μ at the activation point and the onset of dynamic slip stage as μ_a and μ_d, respectively. The variations in μ_a and μ_d with varying σ_{3t} for the fractures with different θ were presented in Figure 15. As the σ_{3t} increased from 10 MPa to 40 MPa, both μ_a and μ_d decreased significantly. For the fractures with θ = 30° and 50°, as the σ_{3t} increased from 10 MPa to 40 MPa, the μ_a decreased from 0.72 to 0.62, and from 0.66 to 0.63, respectively, with weakening rates of 13.99% and 3.98%, respectively. It means that the increasing θ weakened the weakening effect of the σ_{3t} on the μ at the activation point. While for the case of μ_d, an opposite variation trend to that of μ_a was observed. As the θ increased from 30° to 40° and then to 50°, the weakening rate of μ caused by the increase of σ_{3t} increased from 13.32% to 19.02%, and then slightly decreased to 18.25%. The increase in θ strengthened the weakening effect of the σ_{3t} on the μ_d. This implies that there is a competitive relationship between the θ and σ_{3t} for the evolution of the frictional behavior of fractures.

3.3 Variations in JRC tensor

The 3D morphology information of the fracture surfaces before and after experiments were shown in Figures 16, 17, respectively.

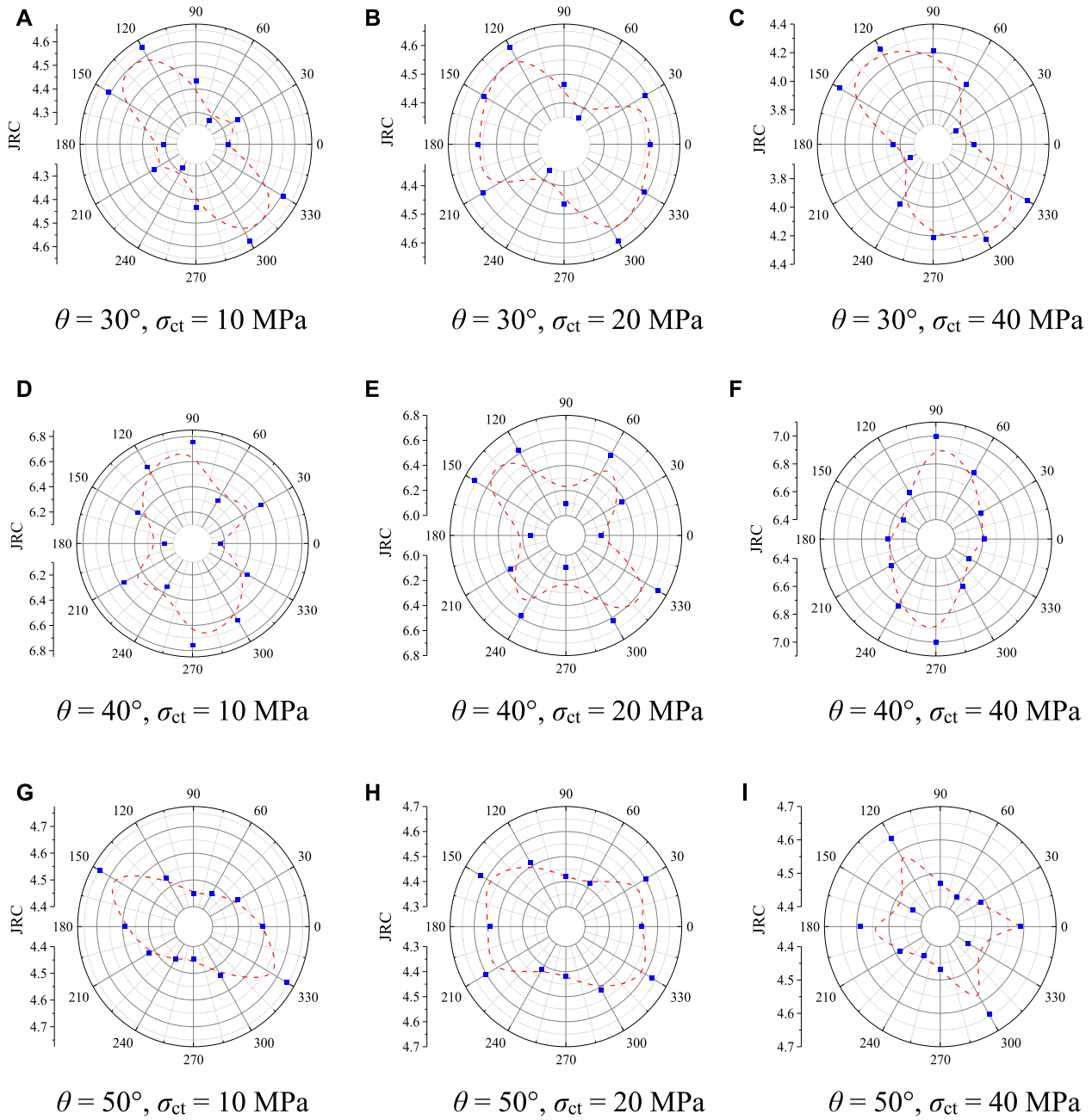

FIGURE 19
Directional JRC contours of fracture surfaces before experiments: **(A)** θ = 30°, σ_{ct} = 10 MPa; **(B)** θ = 30°, σ_{ct} = 20 MPa; **(C)** θ = 30°, σ_{ct} = 40 MPa; **(D)** θ = 40°, σ_{ct} = 10 MPa; **(E)** θ = 40°, σ_{ct} = 20 MPa; **(F)** θ = 40°, σ_{ct} = 40 MPa; **(G)** θ = 50°, σ_{ct} = 10 MPa; **(H)** θ = 50°, σ_{ct} = 20 MPa; **(I)** θ = 50°, σ_{ct} = 40 MPa.

After experiments, the asperities on the fracture surfaces were damaged to a certain extent, which led to the reduction in the elevation of fracture surfaces. The damage degree of the fracture surfaces at the ending of the fractures was significantly severer than that of other regions. Figure 18 depicted the sheared-off thickness of the fracture surfaces in the rectangular region in Figure 16. With increasing θ, the mean value of the sheared-off thickness gradually decreased. As the θ increase from 30° to 50°, for σ_{3t} = 10 MPa, the mean sheared-off thickness decreased from 0.502 mm to 0.433 mm, while for σ_{3t} = 40 MPa, the mean sheared-off thickness decreased from 0.505 mm to 0.319 mm.

In order to realize the quantification of the roughness of fracture surface, the widely accepted joint roughness coefficient (JRC) was used, which can be calculated as (Ji et al., 2023; Zhu et al., 2023):

$$\mathrm{JRC} = 32.2 + 32.47\log Z_2 \tag{9}$$

$$Z_2 = \left[\frac{1}{N}\sum\left(\frac{z_{i-1} - z_i}{y_{i-1} - y_i}\right)^2\right]^{1/2} \tag{10}$$

where N is the quantity of the sample points along the y direction in the 2D cutting line, z_i and y_i are the coordinate in the Cartesian

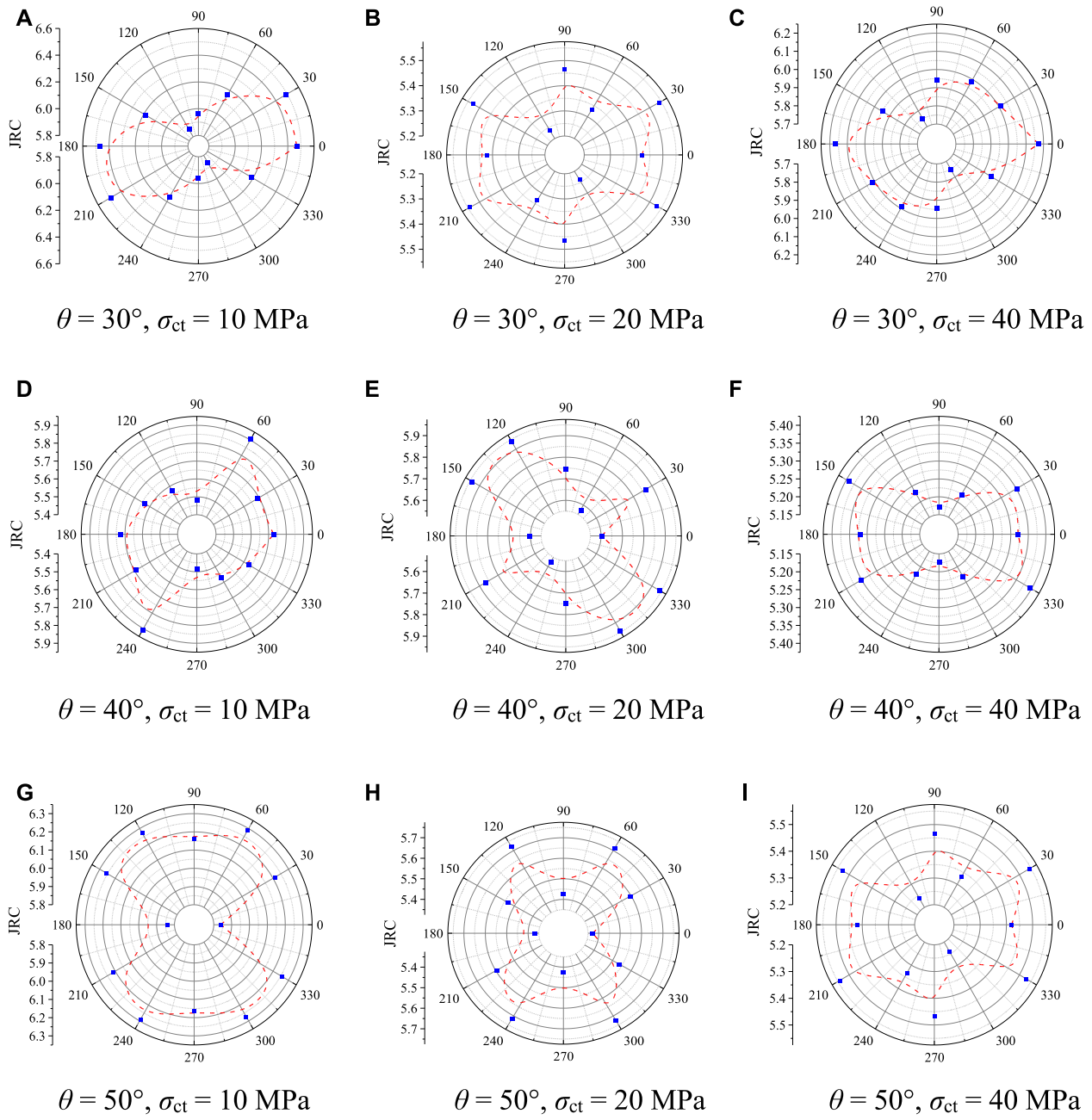

FIGURE 20
Directional JRC contours of fracture surfaces after experiments: **(A)** θ = 30°, σ_{ct} = 10 MPa; **(B)** θ = 30°, σ_{ct} = 20 MPa; **(C)** θ = 30°, σ_{ct} = 40 MPa; **(D)** θ = 40°, σ_{ct} = 10 MPa; **(E)** θ = 40°, σ_{ct} = 20 MPa; **(F)** θ = 40°, σ_{ct} = 40 MPa; **(G)** θ = 50°, σ_{ct} = 10 MPa; **(H)** θ = 50°, σ_{ct} = 20 MPa; **(I)** θ = 50°, σ_{ct} = 40 MPa.

coordinate system. Previous studies have shown that the JRC is anisotropic, nonuniform, and inhomogeneous (Du et al., 2009; Chen et al., 2017; Yong et al., 2019). Since the JRC is calculated as the relative undulation between two adjacent points on the cutting lines of the fracture surfaces, the JRC is equal along two opposite directions. Here, the JRC of the fracture surfaces was calculated along 6 different directions. Assuming that the angle along the positive direction of the *y*-axis is 0° and along the counterclockwise direction is positive, the directions in 0°, 30°, 60°, 90°, 120° and 150° were selected, and eventually the JRC tensors of the nine fracture surfaces were obtained.

As shown in Figures 19, 20, the directional JRC contours with varying directions were plotted. For most of the fracture surfaces, the JRC along the *x* direction was greater than that along the *y* direction after the experiments. This may be due to the fact that the many scratches were generated on the fracture surfaces along the *y* direction or the shearing direction. Under the constant σ_{3t}, the variation in the directional JRC contours can be observed with the increase of θ. When σ_{3t} = 10 MPa, for the fractures with θ = 30°, 40°, 50°, the JRC along the directions of 0° and 90° were 6.47 and 5.96, 5.73 and 5.48, and 5.84 and 6.16, respectively. As the θ increased from 30° to 50°, the ratio of the calculated JRC along the 0° and 90° is

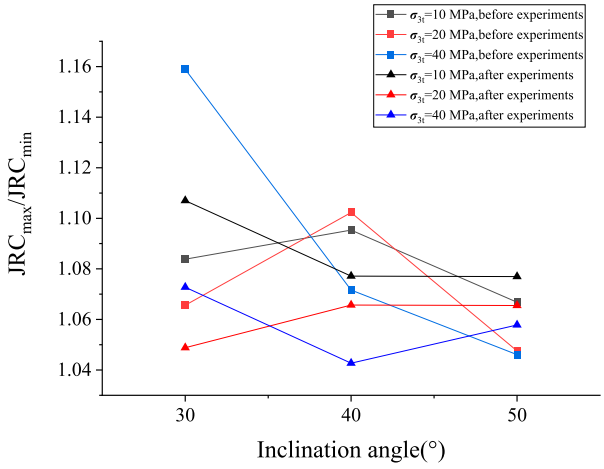

FIGURE 21
Effects of θ and σ_{ct} on the evolutions of JRC_{max}/JRC_{min} before and after the experiments.

reduced from 1.08 to 0.95 for σ_{3t} = 10 MPa, and decreased from 1.04 to 0.99 for σ_{3t} = 40 MPa. Figure 21 shows the ratio (JRC_{max}/JRC_{min}) of the maximum of the directional JRC to the minimum of the directional JRC with varying the θ, and this ratio can well reflect the anisotropy of JRC. The JRC_{max}/JRC_{min} of most fractures showed a slight decrease after experiencing the slipping process. It may be caused by the shearing and crushing processes between asperities. Additionally, the increase in θ may worsen the anisotropy of JRC. For the fracture surfaces after experiments, as the θ increased from 30° to 50°, for σ_{3t} = 10 MPa, 20 MPa, and 40 MPa, the JRC_{max}/JRC_{min} decreased from 1.084 to 1.048, increased from 1.049 to 1.077, and decreased from 1.073 to 1.058, respectively.

3.4 Mechanism of fracture slip and implication for shale gas exploitation

The σ_{3t} and θ have significant effects on the slip and frictional behaviors of fractures. The σ_{3t} controls the slip modes of fractures, and the θ affects the occurrence of the stick-slip events during the quasi-static slip stage. With increasing σ_{3t}, the σ_n applied on fractures increased accordingly, which results in the change in the interaction modes between asperities during the slip process. With the increment of σ_{3t}, the void spaces between the upper and lower asperities were further compacted, resulting in the transition of asperities interaction from overriding mode to sheared-off mode. For σ_{3t} = 10 MPa, the small σ_n corresponds to the asperities that cannot be interlocked and a few of asperities were sheared-off. A large number of intact asperities are still able to act as the obstacles to prevent the slip of the fractures, thus resulting in a large μ_a or μ_d. For σ_{3t} = 20 MPa, amounts of asperities were sheared-off or destroyed due to the large σ_n. Only a few of broken asperities were used to bear the τ, thus leading to great reductions in μ_a and μ_d. When the asperities were sharply sheared off, the sudden release of fracture energy promoted the occurrence of stick-slip events. For σ_{3t} = 40 MPa, most of the asperities were sheared-off when the fractures were activated to slip. Therefore, once the fractures were activated, the fractures would slip at a fast velocity. The sheared-off rock particles produced a lot of fault gouges after crushing. The fault gouges acted as the lubricant in the slipping process, and the presence of fault gouges results in that the μ tended to be stable after a large d_s was generated. Therefore, the μ_a and μ_d were further weakened.

In shale gas production projects, shallow fractures or faults are more likely to be activated due to the small confining pressure. The shear displacement generated after fault activation brings about the release of the accumulated strain energy. However, for fractures under high confining pressure, fractures will not be activated easily and always remain in a stable state. However, once the fractures are activated, a very large amount of strain energy is released. The fractures may slip with a large velocity, and thus leading to a large shear displacement. The duration of this process is shorter than that under small confining pressures. Earthquakes may be induced due to the release of huge amounts of energy in a short period of time. At the same time, before hydro-fracturing, geological exploration should be carried out to determine the strike and dip angle of the main faults. By adjusting the strategy of hydro-fracturing, the appropriate fracturing angle should be adopted to promote the occurrence of stick-slip events. In this way, the earthquakes with large seismic moments may be effectively mitigated.

4 Conclusion

In the study, the triaxial unloading-induced fracture slip experiments were performed to investigate the influences of inclination angle θ and confining pressure σ_{3t} on the slip behavior, friction property and the JRC variation. The slip mechanism of fracture was revealed and the implications were proposed for the safe exploitation of shale gas.

The results show that the slipping process of fractures can be divided into activation stage, quasi-static slip stage and dynamic slip stage. The σ_{3t} controls the slip modes of fractures, while the θ affects the occurrence of the stick-slip events during the quasi-static slip stage. With the increase in σ_{3t}, the main slip modes of fracture transform from the stable-slip to stick-slip, and eventually to the creep-slip. As the θ increased from 30° to 50°, the number of stick-slip events increased from 0 to 3 and from 2 to 4 for σ_{3t} = 10 MPa and 20 MPa, respectively. For σ_{3t} = 40 MPa, all of the three fractures were in a creep-slip state before the activation point and then slipped with a large velocity until it becomes unstable. Thus, no stick-slip event occurred in the slipping process. The increment of θ led to the increase in the duration of quasi-stick slip stage. For σ_{3t} = 10 MPa, the duration of quasi-static slip stage increased from 4.00 s to 1378.67 s as the θ increased from 30° to 50°. The θ and σ_{3t} have great effects on interaction modes between asperities, which directly affected the friction properties of fractures. With increasing σ_{3t}, the void spaces between the asperities were further compacted, resulting in the transition of asperity interaction from overriding mode to shear-off mode. The transition of asperity interaction model therefore brought about the weakening of friction coefficient at the activation point and the onset of dynamic slip stage. For the fractures with θ = 30° and 50°, as the σ_{3t} increased from 10 MPa to 40 MPa, the

μ_a decreased from 0.72 to 0.62, and from 0.66 to 0.63, respectively, with weakening rates of 13.99% and 3.98%, respectively. While for the case of μ_d, an opposite variation trend to that of μ_a was observed. As the θ increased from 30° to 40° and then to 50°, the weakening rate of μ caused by the increase of σ_{3t} increased from 13.32% to 19.02%, and then slightly decreased to 18.25%. The increase in θ strengthened the weakening effect of the σ_{3t} on the μ_d. This implies that there is a competitive relationship between the θ and σ_{3t} for the evolution of the frictional behavior of fractures. As the θ increase from 30° to 50°, for σ_{3t} = 10 MPa, the mean sheared-off thickness decreased from 0.502 mm to 0.433 mm, while for σ_{3t} = 40 MPa, the mean sheared-off thickness decreased from 0.505 mm to 0.319 mm. The increase in θ may worsen the anisotropy of JRC. By adjusting the fracturing angle of hydro-fracturing, the earthquakes with large seismic moments may be effectively mitigated.

In the future, our studies will focus on the slip characteristics of shale fractures through injecting the pressurized fluid. The thermal effect due to the increment of buried depth will also be incorporated.

Data availability statement

The original contributions presented in the study are included in the article/Supplementary Material, further inquiries can be directed to the corresponding author.

Author contributions

YL: Data curation, Formal Analysis, Investigation, Methodology, Project administration, Resources, Software, Visualization, Writing–original draft, Writing–review and editing. ZL: Data curation, Formal Analysis, Investigation, Methodology, Software, Visualization, Writing–original draft, Writing–review and editing. SZ: Conceptualization, Resources, Validation, Writing–review and editing. JJ: Conceptualization, Data curation, Project administration, Resources, Supervision, Validation, Visualization, Writing–review and editing. CY: Conceptualization, Formal Analysis, Funding acquisition, Investigation, Methodology, Project administration, Resources, Supervision, Validation, Visualization, Writing–review and editing.

Funding

The author(s) declare that no financial support was received for the research, authorship, and/or publication of this article.

Conflict of interest

Author YL was employed by Jinan Rail Transit Group Co. Ltd.

The remaining authors declare that the research was conducted in the absence of any commercial or financial relationships that could be construed as a potential conflict of interest.

Publisher's note

References

An, M., Zhang, F., Chen, Z., Elsworth, D., and Zhang, L. (2020b). Temperature and fluid pressurization effects on frictional stability of shale faults reactivated by hydraulic fracturing in the Changning block, southwest China. *J. Geophys. Res. Solid Earth* 125 (8), e2020JB019584. doi:10.1029/2020jb019584

An, M., Zhang, F., Elsworth, D., Xu, Z., Chen, Z., and Zhang, L. (2020a). Friction of Longmaxi shale gouges and implications for seismicity during hydraulic fracturing. *J. Geophys. Res. Solid Earth* 125 (8), e2020JB019885. doi:10.1029/2020jb019885

Bao, X., and Eaton, D. W. (2016). Fault activation by hydraulic fracturing in western Canada. *Science* 354 (6318), 1406–1409. doi:10.1126/science.aag2583

Bijay, K. C., and Ghazanfari, E. (2021). Geothermal reservoir stimulation through hydro-shearing: an experimental study under conditions close to enhanced geothermal systems. *Geothermics* 96, 102200. doi:10.1016/j.geothermics.2021.102200

Brady, B. H., and Brown, E. T. (2006). *Rock mechanics: for underground mining*. Springer science & business media.

Chattopadhyay, A., Bhattacharjee, D., and Srivastava, S. (2020). Neotectonic fault movement and intraplate seismicity in the central Indian shield: a review and reappraisal. *J. Mineralogical Petrological Sci.* 115 (2), 138–151. doi:10.2465/jmps.190824b

Chen, B., Barboza, B. R., Sun, Y., Bai, J., Thomas, H. R., Dutko, M., et al. (2021a). A review of hydraulic fracturing simulation. *Archives Comput. Methods Eng.* 29, 1–58. doi:10.1007/s11831-021-09653-z

Chen, J., Ye, J., and Du, S. (2017). Scale effect and anisotropy analyzed for neutrosophic numbers of rock joint roughness coefficient based on neutrosophic statistics. *Symmetry* 9 (10), 208. doi:10.3390/sym9100208

Chen, Y., Xu, J., Peng, S., Jiao, F., Chen, C., and Xiao, Z. (2021b). Experimental study on the acoustic emission and fracture propagation characteristics of sandstone with variable angle joints. *Eng. Geol.* 292, 106247. doi:10.1016/j.enggeo.2021.106247

Du, S., Hu, Y., and Hu, X. (2009). Measurement of joint roughness coefficient by using profilograph and roughness ruler. *J. Earth Sci.* 20 (5), 890–896. doi:10.1007/s12583-009-0075-3

Elsworth, D., Spiers, C. J., and Niemeijer, A. R. (2016). Understanding induced seismicity. *Science* 354 (6318), 1380–1381. doi:10.1126/science.aal2584

Evensen, D., Varley, A., Whitmarsh, L., Devine-Wright, P., Dickie, J., Bartie, P., et al. (2022). Effect of linguistic framing and information provision on attitudes towards induced seismicity and seismicity regulation. *Sci. Rep.* 12 (1), 11239. doi:10.1038/s41598-022-15448-4

Ferguson, B., Agrawal, V., Sharma, S., Hakala, J. A., and Xiong, W. (2021). Effects of carbonate minerals on shale-hydraulic fracturing fluid interactions in the marcellus shale. *Front. Earth Sci.* 9, 695978. doi:10.3389/feart.2021.695978

Gao, S., Dong, D., Tao, K., Guo, W., Li, X., and Zhang, S. (2021). Experiences and lessons learned from China's shale gas development: 2005–2019. *J. Nat. Gas Sci. Eng.* 85, 103648. doi:10.1016/j.jngse.2020.103648

Giorgetti, C., Tesei, T., Scuderi, M. M., and Collettini, C. (2019). Experimental insights into fault reactivation in gouge-filled fault zones. *J. Geophys. Res. Solid Earth* 124 (4), 4189–4204. doi:10.1029/2018jb016813

Guglielmi, Y., Cappa, F., Avouac, J. P., Henry, P., and Elsworth, D. (2015). Seismicity triggered by fluid injection–induced aseismic slip. *Science* 348 (6240), 1224–1226. doi:10.1126/science.aab0476

Huang, J., Hua, W., Li, D., Chen, X., You, X., Dong, S., et al. (2023). Effect of confining pressure on the compression-shear fracture properties of sandstone. *Theor. Appl. Fract. Mech.* 124, 103763. doi:10.1016/j.tafmec.2023.103763

Huang, N., Liu, R., Jiang, Y., and Cheng, Y. (2021). Development and application of three-dimensional discrete fracture network modeling approach for fluid flow in fractured rock masses. *J. Nat. Gas Sci. Eng.* 91, 103957. doi:10.1016/j.jngse.2021.103957

Ishibashi, T., Elsworth, D., Fang, Y., Riviere, J., Madara, B., Asanuma, H., et al. (2018). Friction-stability-permeability evolution of a fracture in granite. *Water Resour. Res.* 54 (12), 9901–9918. doi:10.1029/2018wr022598

Ji, H., Liu, R., Yu, L., and Zhu, X. (2023). Influence of joint inclination on mechanical behaviors of shales during unloading-induced slip processes. *Int. J. Rock Mech. Min. Sci.* 170, 105487. doi:10.1016/j.ijrmms.2023.105487

Ji, Y., Hofmann, H., Rutter, E. H., xiao, F., and Yang, L. (2022). Revisiting the evaluation of hydraulic transmissivity of elliptical rock fractures in triaxial shear-flow experiments. *Rock Mech. Rock Eng.* 55 (6), 3781–3789. doi:10.1007/s00603-022-02797-9

Ji, Y., Hofmann, H., Rutter, E. H., and Zang, A. (2022). Transition from slow to fast injection-induced slip of an experimental fault in granite promoted by elevated temperature. *Geophys. Res. Lett.* 49 (23), e2022GL101212. doi:10.1029/2022gl101212

Ji, Y., Wu, W., and Zhao, Z. (2019). Unloading-induced rock fracture activation and maximum seismic moment prediction. *Eng. Geol.* 262, 105352. doi:10.1016/j.enggeo.2019.105352

Jia, Y., Song, C., and Liu, R. (2022). The Frictional restrengthening and permeability evolution of slipping shale fractures during seismic cycles. *Rock Mech. Rock Eng.* 55 (4), 1791–1805. doi:10.1007/s00603-021-02751-1

Lade, P. V., and De Boer, R. (1997). The concept of effective stress for soil, concrete and rock. *Geotechnique* 47 (1), 61–78. doi:10.1680/geot.1997.47.1.61

Lee, J. Y., Weingarten, M., and Ge, S. (2016). Induced seismicity: the potential hazard from shale gas development and CO 2 geologic storage. *Geosciences J.* 20, 137–148. doi:10.1007/s12303-015-0030-5

Li, L., Tan, J., Wood, D. A., Zhao, Z., Becker, D., Lyu, Q., et al. (2019). A review of the current status of induced seismicity monitoring for hydraulic fracturing in unconventional tight oil and gas reservoirs. *Fuel* 242, 195–210. doi:10.1016/j.fuel.2019.01.026

Liu, B., Liu, Z., Zhang, M., Xu, J., and Hao, L. (2023c). Triaxial direct shear properties, cohesive damage behavior and shear constitutive model of sandstone under high confining pressure. *Eur. J. Environ. Civ. Eng.* 28, 1284–1299. doi:10.1080/19648189.2023.2248615

Liu, R., Zhu, X., Zhang, Y., Jiang, Y., and Li, S. (2023a). Simultaneous unloading of shear and normal stresses induces activation of naturally rough-walled sandstone fractures. *Int. J. Rock Mech. Min. Sci.* 170, 105488. doi:10.1016/j.ijrmms.2023.105488

Liu, S., Gai, H., and Cheng, P. (2023b). Technical scheme and application prospects of oil shale *in situ* conversion: a review of current status. *Energies* 16 (11), 4386. doi:10.3390/en16114386

Liu, Z., Bai, B., Tang, J., Xiang, Z., Zeng, S., and Qu, H. (2021). Investigation of slickwater effect on permeability of gas shale from longmaxi formation. *Energy & Fuels* 35 (4), 3104–3111. doi:10.1021/acs.energyfuels.0c04081

Ma, Z., Pi, G., Dong, X., and Chen, C. (2017). The situation analysis of shale gas development in China-based on Structural Equation Modeling. *Renew. Sustain. Energy Rev.* 67, 1300–1307. doi:10.1016/j.rser.2016.06.085

Mei, C., and Wu, W. (2021). Fracture asperity evolution during the transition from stick slip to stable sliding. *Philosophical Trans. R. Soc. A* 379 (2196), 20200133. doi:10.1098/rsta.2020.0133

Nur, A., and Byerlee, J. (1971). An exact effective stress law for elastic deformation of rock with fluids. *J. Geophys. Res.* 76 (26), 6414–6419. doi:10.1029/jb076i026p06414

Passelègue, F. X., Brantut, N., and Mitchell, T. M. (2018). Fault reactivation by fluid injection: controls from stress state and injection rate. *Geophys. Res. Lett.* 45 (23), 12–837. doi:10.1029/2018gl080470

Proctor, B., Lockner, D. A., Kilgore, B. D., Mitchell, T. M., and Beeler, N. M. (2020). Direct evidence for fluid pressure, dilatancy, and compaction affecting slip in isolated faults. *Geophys. Res. Lett.* 47 (16), e2019GL086767. doi:10.1029/2019gl086767

Shi, Z., Chen, J., Gong, D., He, S., Jiang, X., Sun, C., et al. (2022). Experimental study on the shear-slip characteristics of natural fractures in shale reservoirs. *Energy Sci. Eng.* 10 (4), 1240–1250. doi:10.1002/ese3.1062

Sun, C., Nie, H., Dang, W., Chen, Q., Zhang, G., Li, W., et al. (2021). Shale gas exploration and development in China: current status, geological challenges, and future directions. *Energy & Fuels* 35 (8), 6359–6379. doi:10.1021/acs.energyfuels.0c04131

Sun, S., Liang, S., Liu, Y., Liu, D., Gao, M., Tian, Y., et al. (2023). A review on shale oil and gas characteristics and molecular dynamics simulation for the fluid behavior in shale pore. *J. Mol. Liq.* 376, 121507. doi:10.1016/j.molliq.2023.121507

Wang, L., Kwiatek, G., Rybacki, E., Bonnelye, A., Bohnhoff, M., and Dresen, G. (2020). Laboratory study on fluid-induced fault slip behavior: the role of fluid pressurization rate. *Geophys. Res. Lett.* 47 (6), e2019GL086627. doi:10.1029/2019gl086627

Wang, L., Zhou, J., Guo, Y., Song, X., and Guo, W. (2022). Laboratory investigation and evaluation of the hydraulic fracturing of marine shale considering multiple geological and engineering factors. *Front. Earth Sci.* 10, 952655. doi:10.3389/feart.2022.952655

Wu, J., Di, Y., Zhang, J., Li, P., Zhang, D., Wang, Y., et al. (2021). Numerical simulation research on influencing factors of post-fracturing flowback of shale gas wells in the Sichuan Basin. *Front. Earth Sci.* 9, 745393. doi:10.3389/feart.2021.745393

Yasuhara, H., Marone, C., and Elsworth, D. (2005). Fault zone restrengthening and frictional healing: the role of pressure solution. *J. Geophys. Res. Solid Earth* 110 (B6). doi:10.1029/2004jb003327

Ye, Z., and Ghassemi, A. (2018). Injection-induced shear slip and permeability enhancement in granite fractures. *J. Geophys. Res. Solid Earth* 123 (10), 9009–9032. doi:10.1029/2018jb016045

Ye, Z., and Ghassemi, A. (2020). Investigation of microseismicity and permeability evolution in shale fractures during stimulation. *SPE Prod. Operations* 35 (04), 0797–0808. doi:10.2118/201115-pa

Yong, R., Gu, L., Ye, J., Du, S. G., Huang, M., Hu, G., et al. (2019). Neutrosophic function with NNs for analyzing and expressing anisotropy characteristic and scale effect of joint surface roughness. *Math. Problems Eng.* 2019, 1–11. doi:10.1155/2019/8718936

Yu, H., Xu, W., Li, B., Huang, H., Micheal, M., Wang, Q., et al. (2023). Hydraulic fracturing and enhanced recovery in shale reservoirs: theoretical analysis to engineering applications. *Energy & Fuels* 37 (14), 9956–9997. doi:10.1021/acs.energyfuels.3c01029

Yuan, J., Luo, D., and Feng, L. (2015). A review of the technical and economic evaluation techniques for shale gas development. *Appl. Energy* 148, 49–65. doi:10.1016/j.apenergy.2015.03.040

Yue, Z., Meng, F., Zhou, X., Wang, X., Zhang, L., and Wang, Z. (2022). Influence of non-persistent joint aperture and inclination angle on the shear behavior and fracture mode of solid rock and concrete material. *Constr. Build. Mater.* 316, 125892. doi:10.1016/j.conbuildmat.2021.125892

Zeng, Y., Ding, S., Chu, Z., Ma, G., Yang, Z., and Gao, S. (2022). Study on shear slip mechanism of shale gas fractured formation. *Petroleum Sci. Technol.* 40 (9), 1123–1137. doi:10.1080/10916466.2021.2013885

Zhang, D., Ranjith, P. G., and Perera, M. S. A. (2016). The brittleness indices used in rock mechanics and their application in shale hydraulic fracturing: a review. *J. petroleum Sci. Eng.* 143, 158–170. doi:10.1016/j.petrol.2016.02.011

Zhang, F., Cui, L., An, M., Elsworth, D., and He, C. (2022). Frictional stability of Longmaxi shale gouges and its implication for deep seismic potential in the southeastern Sichuan Basin. *Deep Undergr. Sci. Eng.* 1 (1), 3–14. doi:10.1002/dug2.12013

Zhang, H., Ren, H., Mu, C., Wu, X., Huang, K., and Wang, F. (2023). Experiment study on the influence of density and confining pressure on triaxial shear properties of calcareous sand. *Materials* 16 (4), 1683. doi:10.3390/ma16041683

Zhang, Q., Hou, B., Lin, B., Liu, X., and Gao, Y. (2021). Integration of discrete fracture reconstruction and dual porosity/dual permeability models for gas production analysis in a deformable fractured shale reservoir. *J. Nat. Gas Sci. Eng.* 93, 104028. doi:10.1016/j.jngse.2021.104028

Zhang, Z., Xu, S., Gou, Q., and Li, Q. (2022). Reservoir characteristics and resource potential of marine shale in South China: a review. *Energies* 15 (22), 8696. doi:10.3390/en15228696

Zhu, X., Ji, H., Liu, R., Yu, L., and Wang, Y. (2023). Numerical study of hydraulic characteristics of shale fractures during unloading-induced slipping: effects of inclination angle and unloading rate. *Comput. Geotechnics* 164, 105811. doi:10.1016/j.compgeo.2023.105811

Zhu, X., Liu, R., Li, W., Qiao, W., Wei, M., and Yu, L. (2024). Correcting the permeability evaluation of elliptical rock fractures in triaxial shear-flow experiments considering channeling flow. *Rock Mech. Rock Eng.* 57 (2), 1509–1523. doi:10.1007/s00603-023-03601-y